

# Water Resources Research®

## RESEARCH ARTICLE

10.1029/2022WR032563

### Key Points:

- Geostatistical Random Mixing simulation now capable of countrywide spatial rainfall interpolation
- Variability assessment via commercial microwave link path consideration and ensemble estimation
- Realistic rainfall pattern representation quantified by ensemble Structure-, Amplitude-, and Location-error metrics

### Supporting Information:

Supporting Information may be found in the online version of this article.

### Correspondence to:

N. Blettner,  
[nico.blettner@kit.edu](mailto:nico.blettner@kit.edu)

### Citation:

Blettner, N., Chwala, C., Haese, B., Hörning, S., & Kunstmann, H. (2022). Combining commercial microwave link and rain gauge observations to estimate countrywide precipitation: A stochastic reconstruction and pattern analysis approach. *Water Resources Research*, 58, e2022WR032563. <https://doi.org/10.1029/2022WR032563>

Received 13 APR 2022  
Accepted 12 OCT 2022

© 2022. The Authors.

This is an open access article under the terms of the [Creative Commons Attribution License](https://creativecommons.org/licenses/by/4.0/), which permits use, distribution and reproduction in any medium, provided the original work is properly cited.

# Combining Commercial Microwave Link and Rain Gauge Observations to Estimate Countrywide Precipitation: A Stochastic Reconstruction and Pattern Analysis Approach

Nico Blettner<sup>1,2</sup> , Christian Chwala<sup>1,2</sup> , Barbara Haese<sup>2</sup> , Sebastian Hörning<sup>3</sup> , and Harald Kunstmann<sup>1,2</sup> 

<sup>1</sup>Institute of Meteorology and Climate Research, Karlsruhe Institute of Technology, Campus Alpin, Garmisch-Partenkirchen, Germany, <sup>2</sup>Chair of Regional Climate and Hydrology, Institute of Geography, University of Augsburg, Augsburg, Germany, <sup>3</sup>Centre for Natural Gas, Faculty of Engineering, Architecture and Information Technology, University of Queensland, Brisbane, Australia

**Abstract** Accurate spatiotemporal precipitation quantification is a crucial prerequisite for hydrological analyses. The optimal reconstruction of the spatial distribution, that is, the rainfall patterns, is particularly challenging. In this study, we reconstructed spatial rainfall on a countrywide scale for Germany by combining commercial microwave link and rain gauge observations for a better representation of the variability and spatial structure of rainfall. We further developed and applied the Random-Mixing-Whittaker-Shannon method, enabling the stochastic reconstruction of ensembles of spatial fields via linear combinations of unconditional random fields. The pattern of rainfall objects is evaluated by three performance characteristics, that is, ensemble Structure-, Amplitude-, and Location-error. Precipitation estimates obtained are in good agreement with the gauge-adjusted weather radar product RADOLAN-RW of the German Weather Service (DWD) which was used as a reference. Compared to reconstructions by Ordinary Kriging, Random Mixing showed clear advantages in the pattern representation via a five times smaller median structure error.

**Plain Language Summary** Rainfall is commonly measured by dedicated sensors such as rain gauges or weather radars. Commercial microwave links (CMLs), which have the primary purpose of signal forwarding within cellular networks, can be used for rainfall measurements too. The signal, which is transmitted from one antenna to another, is being attenuated if it rains along the path. From the amount of attenuation an average rain rate can be retrieved. For many hydrological applications, it is of major interest to estimate area-wide rainfall (i.e., rainfall maps) while observations provide only scattered information. In this study, we used the local information from almost 1,000 rain gauges and the information along the paths of 3,900 CMLs distributed over Germany to reconstruct rainfall maps. We did this by applying a method of stochastic simulation (called Random Mixing) which we compared to a more common method of estimation (Ordinary Kriging). To evaluate the quality of the obtained maps, we compared them to rainfall information from weather radars. We found that the general agreement is high, and that maps reconstructed by Random Mixing have particular advantages in representing the spatial structure, that is, the shape of rainfall cells.

## 1. Introduction

Precipitation is a key feature of the water cycle. Its quantification is crucial for various hydrometeorological applications. At the same time, precipitation is particularly variable in space and time, which makes quantitative estimation on high spatiotemporal resolutions difficult. Since simulations from numerical weather models cannot produce such high-quality quantification, the primary information sources are observations. These observations may suffice with regard to temporal resolution; however, the spatial coverage is generally limited. For hydrological applications such as runoff models, it is crucial to capture the spatial distribution, that is, the pattern of precipitation, accurately.

Common observational data comprises dedicated sensors such as rain gauges and weather radars. Despite some limitations, for example, wind-related underestimation (Pollock et al., 2018) and limited spatial coverage, rain gauges can be considered very accurate precipitation sensors. Weather radars provide a high spatial resolution but have other disadvantages stemming from beam blockage, ground clutter, the measuring height above ground, and the sensitivity to the drop size distribution (Berne & Krajewski, 2013).

Additionally, opportunistic sensors can be used for precipitation estimation. Commercial microwave links (CMLs), operated by mobile communication providers, have been used for rainfall estimation for many years (Leijnse et al., 2007; Messer, 2006). One of the major advantages of CMLs is their widespread presence across the globe. Moreover, rain rate retrieval for typical CML frequencies is, in contrast to radar, rather independent of the drop size distribution. However, as CMLs are not designed and operated with the aim of measuring rainfall, careful processing is required to deduce rainfall information from the raw attenuation (Chwala et al., 2012; Graf et al., 2020; Overeem et al., 2016).

In this study, we use rain gauge and CML observations to calculate spatially interpolated rainfall estimates. Rain gauges represent networks of point observations for which there exist various interpolation methods such as Kriging and inverse distance weighting. CML observations, in contrast, are path-integrated measurements. There is no optimal way to account for such spatially variable nonlocalized measurements in standard interpolation methods. Nevertheless, CML data has successfully been used to estimate rainfall fields in several studies. Overeem et al. (2013) used Ordinary Kriging to derive rainfall maps for the Netherlands, and Graf et al. (2020) used an inverse distance weighting approach to calculate such maps for Germany. In these cases, CML information was reduced to a single point at the center of the CML path. A way to account for the path-averaged nature of CML observations was presented by Goldshtein et al. (2009). They applied inverse distance weighting using virtual rain gauges along the CML paths combined with an algorithm that allows redistribution of rainfall values between the virtual gauges. Other studies that fully take into account the CML observations as path-averaged used tomographic reconstruction (D'Amico et al., 2016; Zinevich et al., 2008) and a block Kriging approach (Graf et al., 2021).

A fundamentally different approach to derive spatial rainfall estimates based on CML and rain gauge data was shown by Haese et al. (2017). Their method of stochastic reconstruction produces rainfall fields with realistic patterns which are constrained by the combination of point and path-averaged observations. For the path-averaged CML observations, the method accounts for the possible variability of rainfall along the paths. It further overcomes the tendency to produce estimates with smoothed spatial gradients which is a general limitation of interpolation methods such as Kriging and inverse distance weighting.

Improved spatial patterns in rainfall field reconstructions are particularly important for the estimation of rainfall at relatively high temporal resolution which is highly variable and intermittent in space. The method used by Haese et al. (2017) has the potential to effectively account for the pattern; however, up to now, it was only applied to small spatial extents and to a limited amount of data.

In this study, we use CML and rain gauge observations distributed over Germany to derive ensembles of rainfall fields via the Random Mixing (Bárdossy & Hörning, 2016) approach similar to the study of Haese et al. (2017). For the first time, we apply this method on a large countrywide scale and for longer periods. This required several smaller adaptations to the method, that is, to make large-scale calculations feasible on a cluster computer, and, to better account for precipitation with high percentages of dry (zero values) observations. Moreover, we focus our study on the evaluation of the quality of reconstructed rainfall patterns using *eSAL* error metrics (Radanovics et al., 2018; Wernli et al., 2008). This allows us to quantify aspects of spatial estimates which cannot be captured by standard performance metrics.

This study aims to answer the following questions: Can we improve large-scale spatial precipitation estimates based on CML and rain gauge data compared to a standard Kriging interpolation? In particular, does our method improve the reconstruction of true spatial precipitation patterns?

## 2. Data and Methods

### 2.1. Data

We used data sets (CMLs and rain gauges) over a period of 3 months, June through August, in 2019. In this section, we first describe a reference data set (gauge-adjusted weather radar) that we use for the validation of our reconstructions, and second, we describe the two data sets which we use as the basis for our reconstructions.

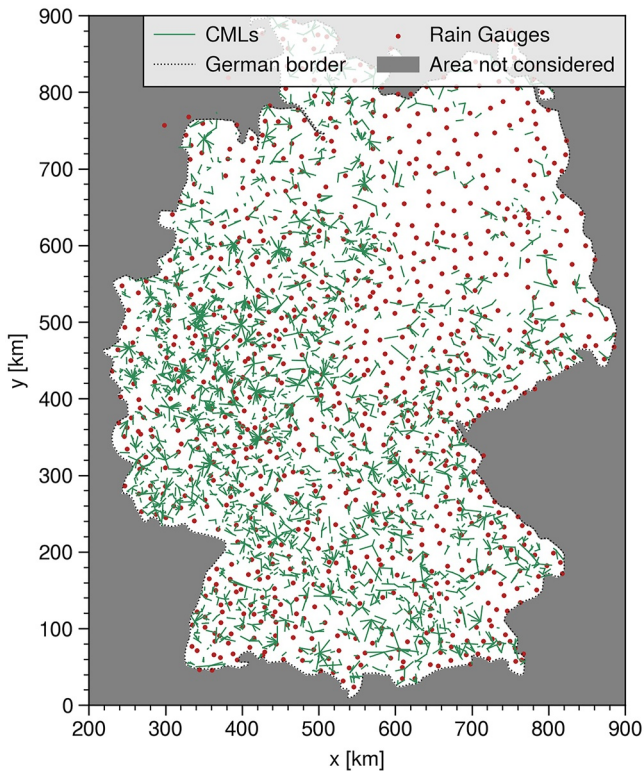


**Figure 1.** Locations of sensors. Areas outside the German borders are not considered in the evaluation.

### 2.1.1. Reference Data RADOLAN-RW

RADOLAN-RW is a product of the German Weather Service (DWD) that provides gridded countrywide precipitation information. It is based on data derived from 17 C-Band weather radars and adjusted to more than 1,000 rain gauges that are distributed over Germany. Each weather radar yields reflectivity observations every 5 min. The information from the individual stations is merged into a national gridded composite using the Python package *wradlib* (Heistermann et al., 2013). Additionally, the 5-min rainfall information is aggregated to full hours and then adjusted to the hourly rain gauge observations by weighted combination of additive and multiplicative correction schemes (Bartels et al., 2004).

The final product yields hourly rainfall sums at time stamps hh:50 and with a precision of 0.1 mm. The spatial extent is a 900-by-900 grid in a stereographic coordinate system covering Germany and parts of the neighboring countries. Each grid cell has a size of 1-by-1 km. For our analysis, we disregard the western margin that is outside the German borders, that is, we consider a grid of 900 km in meridional ( $y$ ) and 700 km in zonal ( $x$ ) direction. Further information on the coordinate system is referenced in the Data Availability Statement.

We are aware of the shortcomings of gauge-adjusted radar products like RADOLAN-RW, stemming from inherent errors of radar rainfall observation and from the imperfect gauge adjustment further away from the gauge locations. However, our analysis requires spatial reference data with high resolution which can only be provided by weather radars. For Germany, RADOLAN-RW, the national operational gauge-adjusted radar product, is thus the reference data set of choice.

### 2.1.2. Data Used for Reconstructions

Our reconstructions are based on rain gauge and CML data. The rain gauges are from the network of the German Weather Service (DWD). The data set

comprises 953 devices that are distributed over Germany (see Figure 1). Note that the rain gauges we use for the reconstructions are also deployed for the radar adjustment. Rainfall sums are recorded every minute. The second data set consists of 3,900 CMLs that are operated by Ericsson. Transmitted and received signal intensities are retrieved in 1-min resolution (Chwala et al., 2016). The CML lengths range between several hundreds of meters and almost 30 km, and their frequencies between 6 and 39 GHz. CML attenuation data requires several processing steps to obtain rainfall information. We apply methods from the Python package *pycomlink* (Chwala et al., 2021) and processing steps according to what is described by Graf et al. (2020). This involves (a) a distinction between wet and dry periods based on the rolling standard deviation of the attenuation time series, (b) an estimation of the baseline attenuation under dry conditions, (c) a correction for the attenuation caused by wet antennas, and (d) the calculation of rain rates from the rain-induced specific attenuation.

We aggregate both rain gauge and CML data to full hours. For consistency with the reference data, we consider hours that start and end at hh:50 (e.g., data from the period between 06:50 and 07:50 is allocated to the time stamp 07:50) as it is done for RADOLAN-RW. The aggregation is only done if there are no missing values in the high-resolution data. For gaps in the original data, we consider the rainfall amount of the affected hour as a missing value. This affects approximately 1.4% and 5.3% of the rain gauge and CML data, respectively. Note that there are whole periods in which almost no CML data is available due to failures of our data acquisition system (see shaded parts in the time series in Figure 2). Those periods are disregarded in the analysis entirely. This reduces the total number of 1-hr time steps from 2,208 (3 months) to 1,885.

The sensor locations are projected onto the polar stereographic coordinate system used for RADOLAN-RW. One of the rain gauges lies outside the grid extent and thus is disregarded. The projection differs slightly between the reconstruction methods applied in this study: For the use in Random Mixing, we project onto the grid points, while keeping the exact (off-grid) values for Kriging.

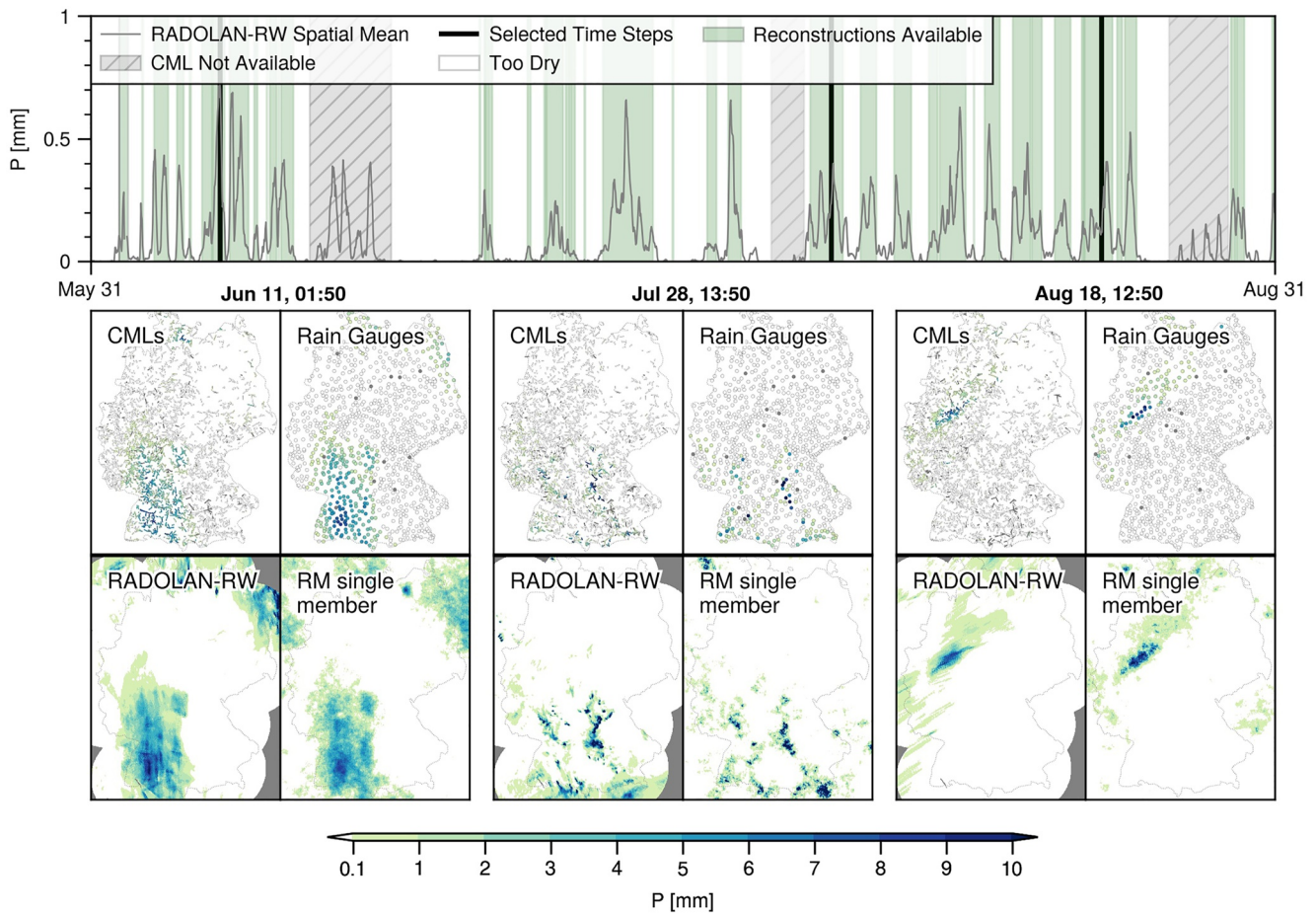


**Figure 2.** Overview of the analyzed period and case studies. Top row: Time series of analyzed period (June–August 2019) including spatial mean rainfall of the RADOLAN-RW reference, and indication where reconstructions were calculated and which time steps were selected for the case studies. Below: For each of the case studies, CML observations, rain gauge observation, RADOLAN-RW data, and a single Random Mixing (RM) reconstruction are shown. Areas that are not covered by RADOLAN-RW as well as observations that did not record values are colored in gray.

We then apply a filtering routine that concerns CML data only, and goes beyond steps described in Graf et al. (2020). It is a spatial sanity check in which single observations at given time steps are excluded from the analysis if they measure values that are distinctly different from the ones of neighboring sensors. As was acknowledged by Graf et al. (2020) and Polz et al. (2020), there still is a considerable amount of false-positive CML rainfall values, despite the advance in CML data processing. Compared to these two studies, we focus on spatial rainfall estimation and an analysis of the derived rainfall patterns. Hence, eliminating spatially isolated false-positive CML rainfall, which impacts its whole surrounding area, has a higher importance in this study. We thus deploy the following heuristic filtering scheme to remove spatially isolated suspicious data points. For any wet (nonzero) observation  $qObs$  we test whether the neighboring observations are all dry. For this, we consider only neighbors in a radius of 15 km. If there exist at least five such neighbors and if they all observe no rainfall, the observation in question  $qObs$  is disregarded. This way, approximately 2.8% of CML data is filtered. Two examples of the effect of this filter can be found in Figures S4 and S5 in Supporting Information S1. Note that this filter is similar to the nearby link approach (Overeem et al., 2016), which has been applied in several studies (e.g., de Vos et al., 2019; Roversi et al., 2020) for identifying wet periods and filtering outliers. An important difference is that our filter uses processed rainfall amounts instead of the raw signal.

We further disregard whole time steps if they are *too dry*, that is, we only consider time steps in which at least five percent of rain gauges and five percent of CMLs record some rainfall. One reason for this is our observation-based estimation of the spatial dependency model which requires a minimum of nonzero observations. Moreover, we are interested in rainfall that covers a considerable spatial extent to allow for a meaningful pattern analysis. This

further reduces the number of total time steps from 1,885 to 819. This disregard of many rather dry time steps limits the applicability to operational use, for which a different approach to the calculation of the spatial dependence model would be required.

## 2.2. Reconstructions

We apply two approaches for the reconstruction of rainfall fields. As the aim of this study is to evaluate the performance of the Random Mixing method for large-scale rainfall estimation, we will give an overview of the basic principles of this method. Before, we shortly first describe the Kriging approach, which we use as a reference method, and afterward, we briefly compare some of the methods' technical aspects.

### 2.2.1. Reference Interpolation Method: Kriging

Kriging is a geostatistical tool that is widely used for spatial interpolation. In this study, we apply Ordinary Kriging (OK) as a reference method. We apply the *PyKrig* Python package (version 1.6.1), with an exponential variogram model and moving window that considers the 10 closest points. The parameters of the variogram are calculated by the package's default L1 norm minimization scheme.

With OK, we can use the rain gauges directly as they are point observations. The CML observations, however, need to be reduced from integral values to point values. Therefore, we assume the CML-derived observations as point measurements at the central positions along the links' paths similar to what was done in Overeem et al. (2013) and Graf et al. (2020).

OK generally allows the creation of values that are outside the range of observations. Hence, we were confronted with nonsensical negative rainfall values which we set to zero before the analysis.

### 2.2.2. Stochastic Reconstruction of Rainfall Fields: Random Mixing

We reconstruct spatial rainfall via the Random Mixing (Bárdossy & Hörning, 2016) approach that is implemented in the Python package *RMWSPy* (Hörning & Haese, 2021). With Random Mixing (RM), we can reconstruct spatial fields, that is, values on a two-dimensional grid, that preserve several features. The spatial dependence structure is obtained from (and thus similar to) that of the rain gauge measurements. Moreover, the marginal distribution of the field is in accordance with the marginal distributions of rain gauge and CML observations. Finally, rain gauge and CML observations can be introduced as linear (localized) and nonlinear (integral) constraints on the field. The following paragraphs are a brief introduction to the methodology. For a detailed step-by-step description of the algorithm, we refer to Hörning and Haese (2021).

The central aspect of RM is the stochastic combination of large numbers  $K$  of unconditional random fields  $Y_i$  with  $i = 1, \dots, K$ . These initial fields are random as they do not account for the observations; however, they represent the spatial dependence structure. Linear combinations of these fields are constructed such that the spatial dependence structure is preserved. To be able to construct such linear combinations, the unconditional random fields  $Y_i$  are required to possess a standard normal value distribution and a spatial dependence structure that can be described by a Gaussian copula (Bárdossy & Hörning, 2016). Let all fields  $Y_i$  have a standard normal marginal distribution, that is, expected values  $E(Y_i) = 0$  and variance  $\text{Var}(Y_i) = 1$ , and a spatial correlation defined by a covariance matrix  $\Gamma$  with  $\Gamma(Y_i)$  equal for all  $Y_i$ . Then we can calculate a linear combination

$$W = \sum_{i=1}^K a_i Y_i. \quad (1)$$

where  $W$  is another spatial field with the same expected value, that is,  $E(W) = 0$ . By ensuring that

$$\sum_{i=1}^n a_i^2 = 1, \quad (2)$$

it follows that also  $\text{Var}(W) = \text{Var}(Y_i) = 1$ . Moreover, Equation 2 guarantees the preservation of the spatial dependence, that is,  $\Gamma(W) = \Gamma(Y_i)$ .

Additionally, the linear combination can be adjusted such that the observational data is represented. Let  $J$  be the number of rain gauges and  $x$  a location on the spatial grid. Rain gauge observations ( $Z(x_j)$ ) with  $j \in [1, \dots, J]$  are first transformed to standard normal space via the transformation

$$W(x_j) = \Phi^{-1}(F(Z(x_j))). \quad (3)$$

where  $F(Z)$  is the marginal distribution of the rainfall deduced from the distributions of rain gauges and CMLs, and  $\Phi^{-1}$  is the inverse standard normal distribution function. Note that we projected the locations such that every rain gauge falls onto a certain grid point, as described in Section 2.1.2. The transformed values are linear constraints and can be fulfilled in Equation 1 if  $K \geq J$ , that is, if the linear equation system is not overdetermined. With  $K > J$  we can additionally account for the validity of Equation 2.

CML observations are nonlinear constraints. To account for them, first the field that is calculated in Equation 1 is back-transformed by the inverse of Equation 3, that is,

$$Z = F^{-1}(\Phi(W)). \quad (4)$$

Then, path-averaged CML observations are compared to  $Z$ . Therefore, we consider the intersecting pixels of  $Z$  for each CML path. These pixels are obtained by the Bresenham Line algorithm connecting the locations of the two poles of a CML. The overall agreement is measured as the Euclidean distance of the differences over all individual CMLs. To adjust the field to CML data, we change the selection of unconditional fields in the linear combination (Equation 1) repeatedly. This iterative approach is governed by the Whittaker-Shannon algorithm which assures convergence and fast computation. For a detailed description of the application of the Whittaker-Shannon algorithm in RM, we refer to Hörning et al. (2019).

RM allows for variability at unobserved locations, that is, at locations without any measurement as well as along the CML paths. Hence, there is not only one solution but we are able to calculate ensembles of reconstructions which allows the quantification of uncertainties. In this study, we calculate an ensemble of 20 single realizations. This number is sufficiently high to see several effects that the ensemble calculation features. At the same time, performance indices are not expected to vary by much for greater ensemble sizes (see Section 4.4) and computational costs which depend on the ensemble size, need to be considered as a limiting factor in RM calculations.

We implemented several adaptations to RM to make the calculations of this study feasible. This comprised the replacement of specific Python packages to speed up the computations. Also, the calibration to CML data was extended such that it can now be done in parallel computing mode. Furthermore, we slightly adapted the treatment of rain gauge observations that recorded no rain. This was necessary as, of course, we needed to cope with many dry observations in the large domain for hourly aggregation times. *RMWSPy*, which is not dedicated to precipitation estimation in particular, involves a special processing for such zero values. The implementation with our adaptations is available on GitHub (see Data Availability Statement below).

### 2.3. Comparison of the Reconstruction Methods

Ordinary Kriging and Random Mixing are fundamentally different methods for spatial reconstruction. While the former yields a most probable estimate at all unknown locations, the latter produces fields that are constrained by local observations and global statistics but involve randomness in the values at unknown locations. In fact, averages over very large RM ensemble sizes converge toward the same output as in OK.

Computationally, RM is clearly more challenging than OK. The time to compute an RM ensemble for one time step was on average 3.8 hr with most time steps requiring less than two but a few even more than 10 hr. The large spread of computation time stems from the optimization algorithm that accounts for the CML observations and which is variable in time. OK, on the contrary, produced solutions (albeit no ensemble) generally in less than a minute per time step. Moreover, RM requires large RAM resources in the case of a large grid as in this study. It computes linear combinations of random fields of which a large enough pool needs to stay in memory. We needed approximately 30 GB of RAM for RM and 1 GB for OK per time step. Note, however, that there exists potential to significantly reduce RM memory usage further, for example, by leaving out areas that can certainly be classified as dry from the calculations of the linear combinations. Such optimization was not the focus of this study, though.

## 2.4. Validation

Our validation comprises two sets of performance metrics. One set that we use for pattern analysis features the consideration of rainfall objects. The other set, which we refer to as standard performance indices, quantifies the quality via pixel-by-pixel comparison. Before calculating the performance metrics, we apply spatial masking of the rainfall maps. First, pixels are set to missing values if they lie outside the German borders (see Figure 1). This means that only about 62% of the 900-by-700 km grid are considered. Second, pixels in the generated rainfall maps are set to missing values at all locations where the reference has missing values. While for most time steps, this affects only 123 (0.03%) of the pixels, in total approximately 0.2% are affected.

### 2.4.1. Pattern Performance Indices: (e)SAL

In this study, we are particularly interested in analyzing rainfall patterns. That is, we assess whether spatial gradients of rainfall amounts are represented in our estimates, and how well one can capture correct shapes, and positions of rainfall objects. To quantify such features, we apply a set of metrics that evaluate deviations in structure  $S$ , amplitude  $A$ , and location  $L$  between a reconstructed and a reference rainfall field. This  $SAL$  analysis, introduced by Wernli et al. (2008), considers properties such as average rainfall amount and centers of mass both for the whole domain as well as for rainfall objects. These objects are defined as connected pixels of the grid with rainfall amounts that exceed a given threshold value. By applying an image processing algorithm, the objects are distinguished from their surrounding. The consideration of rainfall cells as separated objects distinguishes  $SAL$  from standard validation methods, and enables a dedicated assessment of the quality of reconstructed rainfall patterns.

The structure error  $S$  is a measure of differences in weighted rainfall amounts of all the rainfall objects. It has a possible value range between  $-2$  and  $2$ , where negative values indicate too peaked objects and positive values too flat objects. The amplitude error  $A$  describes the discrepancy of domain-averaged rainfall. Similar to  $S$ ,  $A$  may range between  $-2$  and  $2$ . Negative values indicate overall underestimation and positive values indicate overestimation. The  $A$  parameter is independent of the individual rainfall objects. The location error  $L$  evaluates the difference in location of reconstructed and reference rainfall. It is defined as the sum of two components ( $L = L_1 + L_2$ ).  $L_1$  quantifies the spatial dislocation of the weighted center of mass over the whole domain, thereby disregarding the rainfall objects.  $L_2$  considers the displacements of single objects to the total center of mass of the same field. The  $L$  parameter ranges from  $0$  (indicating no location error) to  $2$  (strong location error). A detailed description and definition of the  $SAL$  parameters can be found in Wernli et al. (2008).

Note that only  $S$  and  $L$  do really give an account on rainfall patterns. Therefore, it is mainly these two parameters that we are interested in. Nevertheless, parameter  $A$  is not disregarded in this analysis. It quantifies a domain-wide property but within a similar value space as the pattern-oriented measures  $S$  and  $L$  and at the same time relates to standard performance indices, that is, the bias (BIAS).

Radanovics et al. (2018) extended the  $SAL$  concept by estimating the three parameters for the validation of ensembles. This  $eSAL$  analysis considers the single ensemble members when estimating the regional properties. The ensemble mean of these properties is used to calculate the three parameters  $eS$ ,  $eA$ , and  $eL$ . For the calculation, either both or only one of reconstruction and reference may be ensembles. In case reconstruction and reference both lack the ensemble dimension,  $eSAL$  is equivalent to  $SAL$ . In the following, we generally refer to the parameters by  $S$ ,  $A$ , and  $L$  (without the leading  $e$ ) for both ensemble (RM) and nonensemble (OK) validation.

As mentioned above, the discrimination of rainfall objects requires a threshold value. We define the threshold value by  $f \times R^{95}$ , where  $f$  is the threshold factor and  $R^{95}$  is the 95 percentile of the domain-wide distribution of rainfall amounts considering wet pixels only. Since its definition is dependent on the rainfall amount, the threshold generally differs between reconstruction and reference. The threshold factor  $f$  is set to

$$f = \max\left(\frac{1}{15}, \frac{0.1\text{mm}}{R_{ref}^{95}}\right) \quad (5)$$

where  $R_{ref}^{95}$  is the 95 percentile rainfall amount of the reference. That is, the threshold factor is equal to  $\frac{1}{15}$ , except for cases where this value would lead to a threshold that is smaller than the lowest nonzero value of the field. The reference data has a precision of  $0.1$  mm and by this definition we ensure that the threshold for the reference field is  $0.1$  mm or higher. Equation 5 is only dependent on the reference field as RM and OK reconstructions, do effectively not have precision limits. The choice of the number  $\frac{1}{15}$  follows the definition of Wernli et al. (2008)

who based it on visual confirmation and a sensitivity analysis. The concept of using the 95 percentile and the definition of the threshold factor depending on the precision follows Radanovics et al. (2018).

Furthermore, the calculation of *SAL* parameters requires a treatment of missing values that are present in the RADOLAN-RW data (see Figure 2), and, by our own definition, at locations outside the German borders (see Figure 1). Missing values cannot be handled by the image processing algorithm that defines the rainfall objects. Therefore, and only for the *SAL* analysis, we set those pixels to zero both in the reference data and the reconstructions. This manipulation of the fields does not corrupt the *SAL* metrics. For the rainfall objects, the pixels are never considered if their value is zero and therefore do not influence the objects' properties. Also, the parameters that consider domain-wide average rainfall ( $A$  and  $L_1$ ) are not corrupted as they are relative measures. There is no difference whether missing values are disregarded or considered as zeros since the number of affected pixels is the same in reconstruction and reference. We experimented with interpolating the rare occurrences of missing values of the reference within the German borders. This would however introduce additional uncertainty, especially since missing values generally occur in connected patches at the edge of the reach of the individual radars. Besides, the experiments showed that the differences in the metrics would be negligible.

Within the scope of this study, we developed the functionality to calculate *SAL* parameters in a Python environment. The code is accessible via GitHub (see Data Availability Statement below).

#### 2.4.2. Standard Performance Indices

We calculate several standard performance indices that are commonly used to evaluate the quality of rainfall maps. They relate reconstructions and references via a pixel-by-pixel comparison. We calculate the Pearson correlation coefficient (PCC), the root-mean-square error (RMSE), and the bias (BIAS) as follows

$$PCC = \frac{cov(R_{rec}, R_{ref})}{\sigma(R_{rec}) \times \sigma(R_{ref})} \quad (6)$$

$$RMSE = \sqrt{\mu((R_{rec} - R_{ref})^2)} \quad (7)$$

$$BIAS = \frac{\mu(R_{rec} - R_{ref})}{\mu(R_{ref})} \quad (8)$$

where  $R_{rec}$  and  $R_{ref}$  are the rainfall amount for all pixels of the reconstruction and the reference, respectively.  $cov(\cdot)$  is the covariance function,  $\sigma(\cdot)$  the standard deviation function, and  $\mu(\cdot)$  the arithmetic mean function.

### 3. Selected Case Studies: Synoptic Situation

Our analysis covers the 3 months June, July, and August 2019. During the summer months, there is generally almost no solid precipitation, but a mixture of convective and stratiform rainfall patterns over Germany. Throughout the country, this summer was characterized by warm and dry conditions. However, several intense rainfall events took place particularly in the southern parts of the country.

In addition to the analysis over the 3-month period, we selected three time steps for a detailed analysis of rainfall patterns. We chose one rainfall event of each analyzed month. Those events differ in terms of rainfall location, type, and synoptic conditions. All three time steps represent synoptic conditions that are rather common in Germany (Werner & Gerstengarbe, 2010).

The first selected time step is of June 11 at 01:50. The synoptic condition at this time was dominated by high pressure over Central Europe. Germany was influenced by anticyclonic patterns. For several days the weather in Germany was characterized by strong thunderstorms which had particular strong severity in southern parts of the country. At the selected time step there was widespread intense rainfall over southwestern Germany and several rainfall cells along the Baltic Sea and the border to Poland.

The second selected time step is of July 28 at 13:50. The conditions were characterized by a high-pressure zone over the Atlantic and low pressure over western Asia. Especially in the southern half of Germany, there were local and partly very intensive convective rainfall cells.

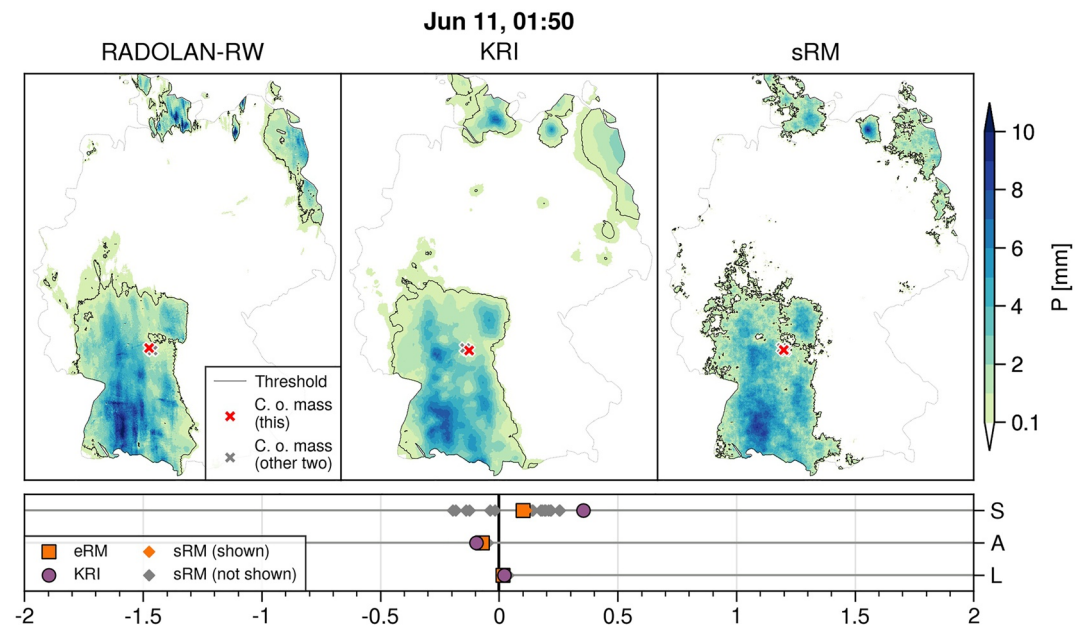


**Figure 3.** Top row: Rainfall maps of first selected time step (June 11, 01:50) for reference, KRI reconstruction, and sRM reconstruction (a single ensemble member), with centers of mass indicated by the crosses, and threshold values that encapsulate the rainfall objects (see Section 2.4.1 for details). Below the maps, the SAL error metrics are shown. The framed squares represent *eSAL* results of eRM, smaller squares represent SAL results of all individual ensemble members, and the circles represent SAL of KRI.

The synoptic condition of the third time step (August 18 at 12:50) was dominated by zonal westerly directions of inflow and a cyclonic regime. There was a center of low pressure over the northern Atlantic between Iceland and the British Isles, and a belt of high pressure reaching from the Azores through central Europe and Germany, to Russia. Over Germany, there was a decline in pressure from the Alps to the North Sea. These conditions led to cyclonic frontal rainfall over northwestern Germany.

## 4. Results and Discussion

Our analysis comprises 815 hourly time steps. We calculated rainfall maps for 819 hourly time steps as described in Section 2 and disregarded 4 time steps in which reference data is not available. Figure 2 shows which time steps of the 3-month periods are considered and gives an overview of observational data, reference data, and an RM reconstruction for the three selected case studies. In this section, we will first present SAL results for these case studies, followed by the SAL statistics for all calculated time steps. Subsequently, we will present the analysis based on standard performance indices, and an analysis of the ensemble means of different ensemble sizes which range between 3 and the total of 20 ensemble members that have been calculated in this study. We generally refer to Random Mixing reconstructions by eRM, sRM, and mRM(*M*) if we consider the whole ensemble, a single ensemble member, or the mean of *M* members, respectively, and Kriging reconstructions by KRI. Note that for the (*e*)SAL analysis, we generally refer to the parameters by *S*, *A*, *L* omitting the leading “*e*.” For eRM, this implies that *S* is actually *eS* (likewise for *A* and *L*), that is, a single value describing the whole ensemble.

### 4.1. SAL Analysis: Case Studies

For the selected time steps, we present rainfall maps of reference, KRI, and one of the sRM reconstructions together with the SAL parameters in Figures 3 and 4. Note that in the case of RM SAL parameters are shown for eRM as well as for sRM. Similar figures showing mRM maps can be found in the supporting material (Figures S1–S3 in Supporting Information S1).

On June 11, 2019 at 01:50 (Figure 3), there was considerable rainfall over southwestern and northeastern Germany. By visual comparison, both the sRM and KRI reconstructions are in good agreement with the reference. The

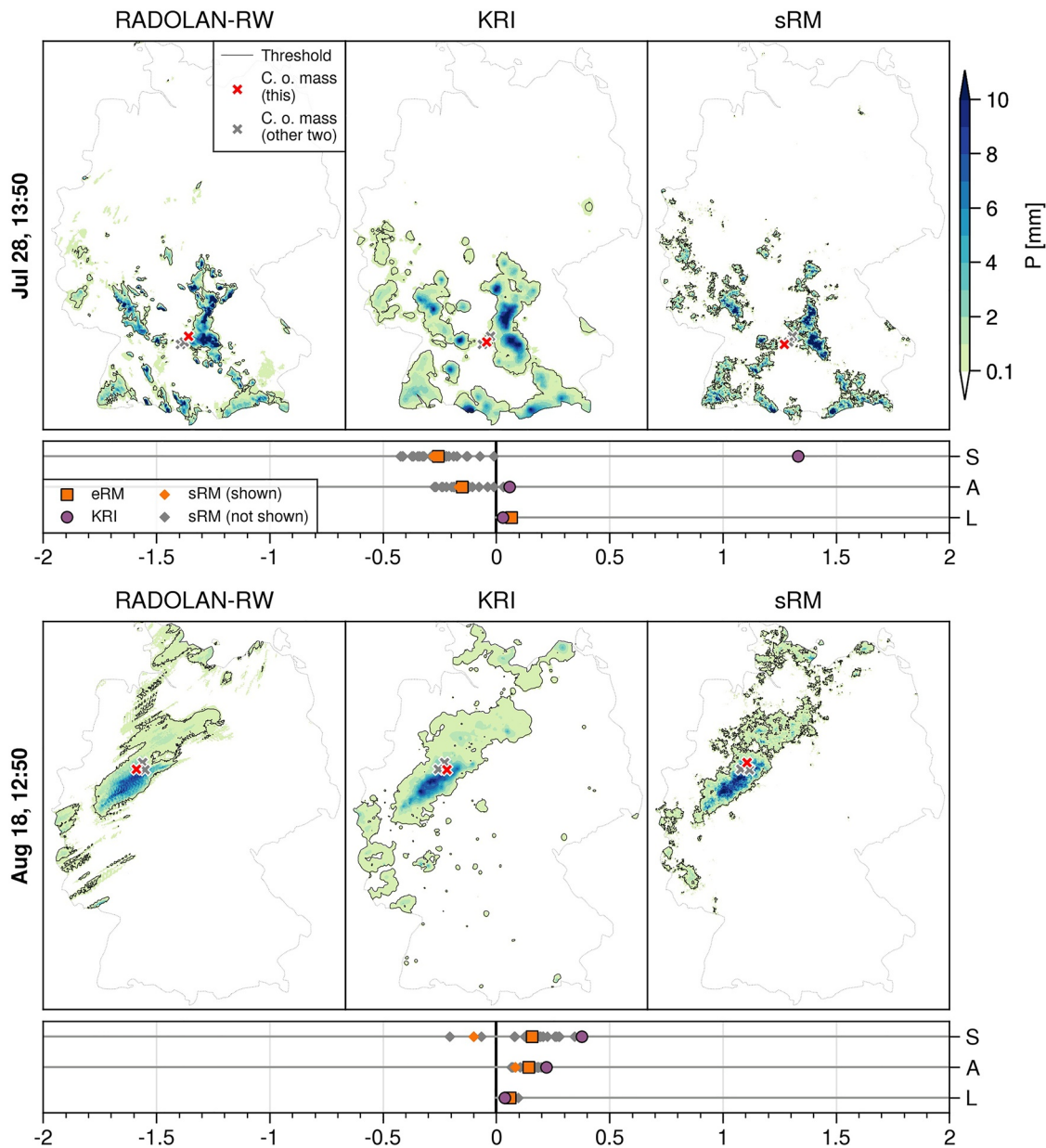


**Figure 4.** Rainfall maps and SAL metrics for second and third selected time steps. The maps show the reference data, a Kriging reconstruction, and a single sRM reconstruction, with centers of mass and threshold values that encapsulate the rainfall objects, for each time step. Below the maps, *eSAL* results for eRM are shown by the framed squares, *SAL* of individual sRM members by the smaller squares, and *SAL* of KRI by the circles (cf. Figure 3).

spatial extent as well as rainfall amounts are well represented in the reconstructions. Comparing sRM and KRI, a general difference in the structure can be seen along the edges of the rainfall objects: KRI objects have straight edges while for sRM they are rather convoluted. This displays a high spatial variability in sRM.

The visual observations can be supported by the *SAL* metrics. (Table S1 in Supporting Information S1 gives an overview of metrics that are discussed in the following.) The *S* parameters for eRM and for KRI are positive which shows that both eRM and KRI produce too widespread or less peaked objects. However, for eRM ( $S = 0.100$ ), this value is clearly smaller than for KRI ( $S = 0.355$ ) which indicates that the structure is better captured in eRM. The tendency for too smooth spatial gradients is implicit in OK as the variability is strongly constrained by local observations. RM, on the other hand, enables a reconstruction that does not involve this tendency.

The  $A$  parameter reveals that the error in representing domain-wide rainfall is small for both eRM and KRI. Both reconstructions suffer from slight underestimations that are similar in magnitude. The amplitude errors for eRM ( $A = -0.072$ ) and KRI ( $A = -0.096$ ) represent approx. 93% and 91% of the reference rainfall, respectively.

The  $L$  parameters show that dislocation is generally small. The domain-wide dislocation measured by  $L_1$  indicates a shift of approx. 10 km for both eRM and KRI (both with  $L_1 = 0.009$ ).

The second selected time step (July 28, 13:50, see upper part in Figure 4) is characterized by several convective cells with large rainfall amounts over southern Germany. As for the first case, the overall picture is captured by the reconstructions. For this time step, we see strong differences in the representation of the rainfall structures between sRM and KRI. sRM represents the small-scale spatial variability and produces many narrow but peaked rainfall objects. KRI, on the other hand, is characterized by much broader objects and less locations with very high rainfall amounts. The sharp spatial gradients observable in convective conditions are not captured in KRI. Instead, fewer features are present that are connected over relatively large extents.

The difference in structure that can be seen in the maps is also represented by the  $S$  parameter which is very high for KRI ( $S = 1.331$ ) and much closer to 0 for eRM ( $S = -0.257$ ). Again, the large structural error demonstrates that rainfall objects are too smooth and widespread in the KRI reconstruction, and confirm that KRI has shortcomings in producing adequate peaks and finer structures.

The amplitude error reveals that KRI represents the overall rainfall amount well. Its  $A$  value of  $-0.058$  relates to a representation of approx. 94% of reference rainfall. For eRM, we observe underestimation ( $A = -0.152$ ) which translates to approx. 86% of reference rainfall.

As in the aforementioned example, the location error is small for both eRM and KRI. The displacement of the total center of mass is toward the south-west for both the shown sRM ensemble member and KRI. The  $L_1$  component of eRM (0.029) and KRI (0.014) indicate dislocations of the total center of mass of approx. 33 and 16 km, respectively.

The last selected time step (August 18, 12:50, see lower part in Figure 4) is characterized by frontal rain that covers the northern parts of Germany. In contrast to the other examples, we observe a clearly anisotropic rainfall pattern, that is, rainfall objects are elongated in SW-NE direction in the reference. The elongation can also be seen in the reconstructions on a large scale. However, on a smaller scale, for example, when focusing on single peaks, the elongation is not well represented in the reconstructions. Moreover, some of the rainfall objects of rather low amplitudes that are visible in the reference are not present in both sRM and KRI. On the other hand, there are several small objects that are present in KRI but not in the reference or sRM. These might be attributed to false positive rainfall values of the CMLs that were missed by the filter we applied (see Section 2.1.2). With regard to the relation of spatial extent, sRM and KRI reconstructions differ substantially. For KRI, a large area is covered by moderate rainfall, while for sRM the spatial extent is smaller but the peaks are higher. Especially in the northern and western parts of the domain, KRI produces widespread objects and sRM several smaller ones.

Similar to both cases discussed above, the structure error is smaller for eRM ( $S = 0.158$ ) than for KRI ( $S = 0.376$ ). The amplitude error is slightly positive and similar for KRI and the eRM. Their values ( $A = 0.220$  for KRI) and ( $A = 0.142$  for eRM) represent approx. 125% and 115% of reference rain, respectively. Location errors for the eRM and KRI are particularly small.

#### 4.2. SAL Analysis: Overall Statistics

The following presents the SAL results for the whole analyzed period. Figure 5 shows boxplots of the parameter distributions for eRM, mRM(20), and KRI over time. Note that the sample sizes of the parameters do not differ among the three cases. While  $S$  of KRI and mRM(20) is mostly strongly positive (median of 0.583 and 0.530, respectively),  $S$  of eRM displays smaller values (median of  $-0.110$ ). This shows the tendency of KRI to produce rather widespread, flat objects, while eRM has only a weak tendency for too peaked objects. mRM(20) is similar to KRI with regard to the structural error. For the  $A$  parameter, there is (by definition) no difference in eRM and mRM(20). From median values of  $-0.159$ , it follows that 85% of the reference rainfall amount is represented by eRM. For KRI, the median  $A$  value is  $-0.035$  which corresponds to approx. 97% of the reference rainfall amount. Compared to  $S$  and  $A$ , the location error is relatively small for eRM, mRM(20), and KRI. Moreover, it shows a narrow range of values. Median values of 0.042 (eRM), 0.057 (mRM(20)), and 0.059 (KRI) reveal a slight

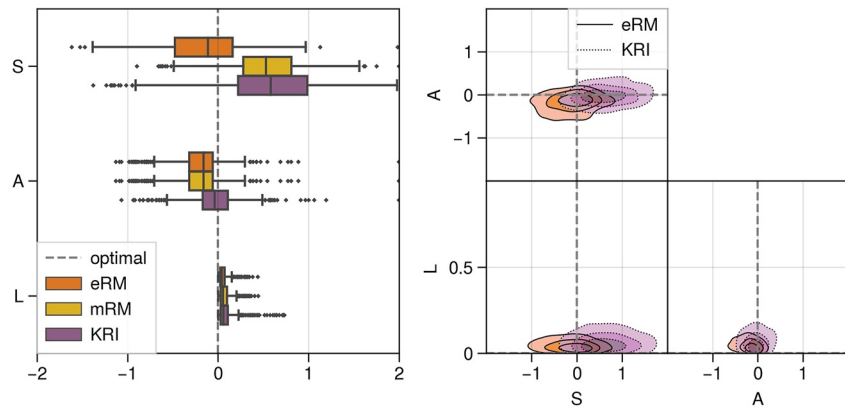
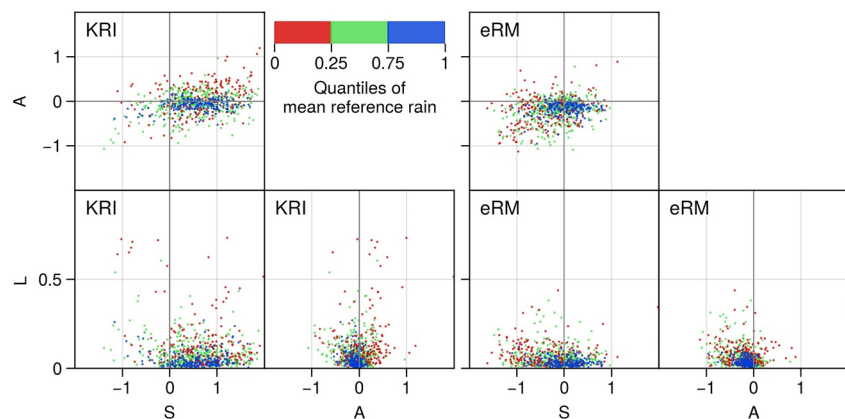


**Figure 5.** Distribution of the SAL metrics for the whole analyzed period. Boxplots for  $eSAL$  of eRM,  $SAL$  of mRM(20), and  $SAL$  of KRI (left); probability density of SAL value distribution in contour plots (right) of  $A$  versus  $S$ ,  $L$  versus  $S$ , and  $L$  versus  $A$ . For each of the reconstructions the outer, middle, and inner contour represent a probability density of 0.25%, 0.5%, and 0.75%, respectively.

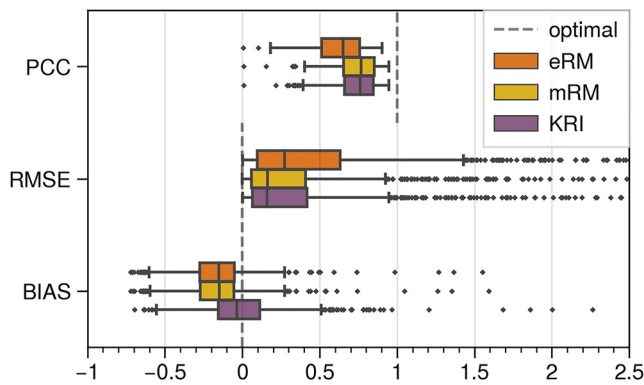
advantage for eRM with regard to representing the location of rainfall. The median  $L_1$  parameter of eRM (and mRM(20)) is 0.021 which corresponds to a distance in the location of the total center of mass of approx. 24 km. For KRI, the median  $L_1$  is only slightly higher (0.023).

Figure 5 also presents the internal mutual dependencies of the three SAL parameters. It should be noted that the SAL parameters are constructed (e.g., by applying field-dependent rainfall threshold values and scaling of objects for the calculation of  $S$ ) such that they measure distinct features and do not exhibit strong correlation. In fact, Figure 5 (right) suggests that the parameters can be considered largely independent from one another.

On the contrary, we find a clear correlation when we consider the overall rainfall amount. Figure 6 shows all data points in the time series colored according to the spatial mean rain of the RADOLAN-RW reference. For all parameters and particularly for  $A$ , we see that time steps with little rain show a larger scatter. Moreover, we observe a small positive correlation between  $A$  and  $S$  in cases with little rainfall. Strong rainfall, on the other hand, is associated with smaller SAL errors and smaller scatter. These observations are similar for eRM and KRI. Since these parameters are relative measures, they are likely to be more sensitive and more correlated under conditions of little total rain.



**Figure 6.** Relation of SAL parameters as scatter plots for all available time steps. For KRI (left) and eRM (right), colored according to rainfall amount. The time steps are put into three categories: 25% time steps with least, 50% with intermediate, and 25% with highest mean rainfall amount of the RADOLAN-RW reference.



**Figure 7.** Pixel-based performance metrics for the whole analyzed period. For eRM, the median of the ensemble is considered.

### 4.3. Analysis by Standard Performance Indices

To put the results from the SAL analysis into perspective, we also analyzed the reconstructions using standard performance indices that are based on a pixel-by-pixel comparison. A summary of these indices for eRM, mRM(20), and KRI is shown in Figure 7. Note that for eRM, we consider the median over the ensemble dimension.

The correlation index  $PCC$  shows a wide range of positive values in all three cases. eRM performs worse than KRI with regard to this metric. The median (over time)  $PCC$  is 0.651 and 0.762 for eRM and KRI, respectively. mRM(20) (median of 0.766), however, shows correlations that are slightly higher than KRI correlations. In a similar manner, eRM generally performs worse than KRI with regard to  $RMSE$ . We see higher errors for eRM (median of 0.274 mm) than for mRM(20) and KRI (median of 0.164 and 0.159 mm, respectively).  $RMSE$  shows a strongly skewed distribution with several outliers that have high errors. The  $BIAS$ , which is directly related to the  $A$  parameter of the  $SAL$  analysis, is similar for eRM and mRM(20) (median of  $-0.151$  and  $-0.147$ , respectively). It is also negative but of lower magnitude for KRI (median of  $-0.034$ ). All the reconstructions show a tendency for underestimation.

The analysis of standard performance indices displays a contrast to the  $SAL$  analysis above, and thereby highlights that metrics based on pixel-by-pixel comparison cannot account for all relevant features of a reconstruction. Focusing on  $PCC$  and  $RMSE$ , KRI has an advantage over eRM. The pattern analysis, on the other hand, suggested that eRM is capable of reproducing the structure better than KRI. In both regards, mRM(20) is closer to KRI than the eRM. That is, the shortcoming of eRM with regard to  $PCC$  and  $RMSE$  is more than compensated when considering mRM(20); however, at the same time, the advantage of eRM with regard to the structure is reduced for mRM(20). So far, we only compared single fields with the mean of the whole ensemble, containing 20 single fields. In the next section, we will present an analysis that takes into account averages over different ensemble sizes.

### 4.4. Analysis of Ensemble Averages

We showed that eRM has benefits over KRI with respect to pattern representation and shortcomings with respect to standard performance indices, and that considering mRM( $M$ ) ensemble means can be used to reduce the differences in both cases. So far, we considered single fields and the mean of the whole ensemble which consists of 20 members. Now we compare the performance of various aggregation sizes  $M \in [1, 3, 5, 10, 20]$  (Figure 8), with mRM(1) being equivalent to sRM. Apart for the case  $M = 20$ , we randomly selected a subset of the ensemble. We tested various combinations of random selections which showed that the selection does result only in negligibly small variance of the metrics. Note that the number of possible combinations is different and can be very large depending on  $M$ , such that the calculation of all combinations is not practicable.

We find that standard metrics like  $PCC$  and  $RMSE$  that indicate a relatively low performance of sRM improve significantly once we consider ensemble mean fields even of small sizes. Both  $PCC$  and  $RMSE$  are very close to KRI for mRM(5) and almost equal for mRM(10). As seen above, mRM(20) already performs slightly better than KRI. However, we also see that the rate of change levels out for the large ensemble sizes. The structure error  $S$ , on the contrary, deteriorates with increasing  $M$ . While it is  $-0.130$  for a single sRM member, it is 0.325 for mRM(5). It further increases for larger  $M$  but levels off, too. In all cases, the structure error of mRM is clearly below  $S$  of KRI. The location error is also the lowest for sRM single fields. It increases slightly for mRM(3) but does not change for larger  $M$ . Besides, it is almost equal to  $L$  of KRI once  $M > 1$ . The  $A$  parameter and the  $BIAS$  are generally not influenced by the ensemble size, and slightly worse for sRM and mRM compared to KRI.

These comparisons highlight the potential that comes with the ensemble calculation in RM. Single fields show better structure representation but worse standard metrics. However, averaging over the ensemble dimension can help to remove the shortcomings of RM with regard to the latter set of metrics. Albeit the structure representation of these ensemble averages is worse than that of RM single fields, it is still better than that of KRI. The ensemble size considered for averaging can be adjusted to specific use cases, depending on which aspect of the field is of

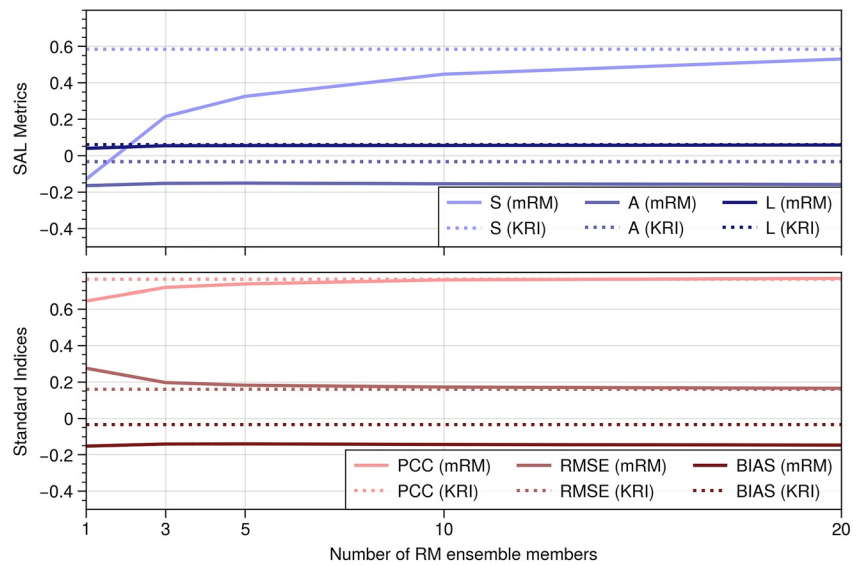


**Figure 8.** Various performance metrics for ensemble mean fields of different ensemble sizes. Solid lines represent mRM and dotted lines KRI. The latter is represented by a single value and not dependent on the ensemble dimension.

most interest. We do not expect large changes in the metrics for ensemble sizes that are greater than the ones we consider in this study, since Figure 8 clearly shows the convergence of the metrics with increasing number of RM ensemble members. Moreover, the size suffices to achieve *PCC* and *RMSE* values for mRM that are similar to KRI. Only the overall underestimation of RM cannot be reduced by averaging over the ensemble dimension.

## 5. Conclusions

We applied the Random Mixing (RM) method for producing countrywide spatial rainfall estimates based on CML and rain gauge data and carried out a validation using (*e*)*SAL*, a specific set of metrics for structure, amplitude, and location of spatial data. We find that RM reconstructions show a reasonable agreement with the reference data. Moreover, when comparing RM reconstructions with Ordinary Kriging (KRI) reconstructions, we find that the former has advantages in reproducing rainfall patterns, while at the same time, the single RM fields showed lower performance than KRI fields when analyzed via standard performance indices.

RM works fundamentally differently than KRI. It does not interpolate observations values in space, but rather generates possible rainfall fields that agree with the observations. The generated rainfall fields follow a specific spatial dependence structure derived from the observations. This explains the much better performance of RM rainfall fields with regard to spatial structures compared to the KRI fields which are always much too smooth. Especially for complex patterns this aspect is crucial. We found the greatest advantage of RM over KRI for the case of convective conditions, where spatial variability is particularly pronounced. However, the fact that RM generates possible rainfall fields can result in large variations further away from the observations which constrain the generation process. Hence, single RM rainfall fields can show large deviations from the reference in regions without observations, leading to relatively weak performance regarding standard metrics. When considering an ensemble of rainfall fields, this variation does, however, reflect the uncertainty of the rainfall field reconstruction.

The possibility of RM to generate an ensemble of possible rainfall fields that fit to the point observations of the rain gauges and the path-averages from CMLs is a major advantage. Considering ensemble averages, we are able to reduce the variability that is present in the single ensemble members. Such averages are similar to a KRI reconstruction with regard to most performance metrics. They show a slightly worse pattern representation, but enhanced pixel-based metrics, compared to single ensemble members. Thus, RM allows the consideration of a spectrum of solutions, from single ensemble members to ensemble averages of various sizes, depending on the application.

A disadvantage of RM observed in this study is its stronger (compared to KRI) tendency for underestimation. This, in contrast to the other analyzed properties of the fields, cannot be influenced by the consideration of ensemble aggregates. However, the underestimation might be minimized by adjustments in the RM algorithm. The estimation of the marginal distribution can probably be optimized and calibrated to reduce this bias. We further observed shortcomings in representing the anisotropy of rainfall objects that might be accounted for in future versions of RM. In spite of these limitations, we could show that RM has the potential to produce valuable estimates that can outperform standard methods depending on the use case.

For certain hydrological models, it might be useful to consider single RM ensemble members that give a true representation of spatial gradients. This allows the assessment of expected spatial extents relative to the total rainfall amount of a rainfall object. That is, RM can reduce overestimation of spatial extents as well as underestimation of peaks. One can further use different ensemble members as model input for the estimation of uncertainties, or consider ensemble averages which are less variable and more conservative.

This shows that with RM, we have a suitable method for precipitation estimation. It is capable of dealing with a combination of different and extensive observational data appropriately, produces fields with high-quality pattern representation, and allows for different perspectives via the consideration of ensemble aggregates.

### Acronyms

RM	Random Mixing, the method generally
eRM	The full ensemble reconstructed using the Random Mixing method
sRM	A single ensemble member of the Random Mixing reconstruction
mRM(M)	The ensemble mean over $M$ ensemble members of the Random Mixing reconstruction
OK	Ordinary Kriging, the method generally
KRI	The reconstruction by Ordinary Kriging
(e)SAL	(Ensemble) Structure, Amplitude, Location Error, also used independently as $S$ , $A$ , and $L$ , or $eS$ , $eA$ , and $eL$
$L_1$	One of two components of the Location Error $L$
PCC	Pearson correlation coefficient based on comparing reconstructions pixel-by-pixel
RMSE	Root mean square error based on comparing reconstructions pixel-by-pixel
BIAS	Relative bias based on comparing reconstructions pixel-by-pixel

### Data Availability Statement

CML data were provided by Ericsson Germany and are not publicly available for reasons of their commercial interest. An individual agreement with the network provider needs to be established to obtain the CML data for research purposes. Rain rate retrieval was conducted using *pycomlink* (Chwala et al., 2021) under BSD-3-Clause License, <https://doi.org/10.5281/zenodo.4810169>. The *pycomlink* repository contains an exemplary CML data set that may be used to follow the methodology of this study. Rain gauge data and RADOLAN-RW data (Bartels et al., 2004) are available from the Climate Data Center of the German Weather Service at ([https://opendata.dwd.de/climate\\_environment/CDC](https://opendata.dwd.de/climate_environment/CDC)). The well-known-text definition of the RADOLAN projection can be found at: (<https://maps.dwd.de/geoserver/web/wicket/bookmarkable/org.geoserver.web.demo.SRSDescriptionPage?10&code=EPSG:1000001>). *PyKriging* which was used for the Kriging reconstructions is available under GNU General Public License (Murphy et al., 2021), <https://doi.org/10.5281/zenodo.5380342>. *RMWSPy* is available under GNU General Public License (Hörning, 2022), <https://doi.org/10.5281/zenodo.7048941>. Adaptions to *RMWSPy* applied in this study are available here: Hörning and Blettner (2022), <https://doi.org/10.5281/zenodo.7049826>. The functionality to calculate eSAL parameters in Python are available at Blettner (2022) under MIT License, <https://doi.org/10.5281/zenodo.7049846>.

### References

- Bárdossy, A., & Hörning, S. (2016). Random mixing: An approach to inverse modeling for groundwater flow and transport problems. *Transport in Porous Media*, 114(2), 241–259. Retrieved from <http://link.springer.com/10.1007/s11242-015-0608-4>
- Bartels, H., Weigl, E., Reich, D. T., Lang, P., Wagner, A., Kohler, O., & Gerlach, N. (2004). Routineverfahren zur Online-Aneicherung der Radarniederschlagsdaten mit Hilfe von automatischen Bodenniederschlagsstationen (Ombrometer).

#### Acknowledgments

The authors thank Ericsson for the cooperation and support in the acquisition of CML data. The authors acknowledge the access to rain gauge and RADOLAN-RW data from the German Weather Service. This work is funded by the German Research Foundation via the Sprail-INK and the FOR2131 projects (Grants CH-1785/2-1 and KU-2090/6-2), and the Federal Ministry of Education and Research via the HoWa-innovative project (Grant 13N14826).

- Berne, A., & Krajewski, W. (2013). Radar for hydrology: Unfulfilled promise or unrecognized potential? *Advances in Water Resources*, 51, 357–366. <https://linkinghub.elsevier.com/retrieve/pii/S0309170812001157>
- Blettner, N. (2022). *nblettner/eSALpy: v1.0.0*. Zenodo. <https://doi.org/10.5281/zenodo.7049846>
- Chwala, C., Gmeiner, A., Qiu, W., Hipp, S., Nienaber, D., Siart, U., et al. (2012). Precipitation observation using microwave backhaul links in the alpine and pre-alpine region of Southern Germany. *Hydrology and Earth System Sciences*, 16(8), 2647–2661. <https://hess.copernicus.org/articles/16/2647/2012/>
- Chwala, C., Keis, F., & Kunstmann, H. (2016). Real-time data acquisition of commercial microwave link networks for hydrometeorological applications. *Atmospheric Measurement Techniques*, 9(3), 991–999. <https://amt.copernicus.org/articles/9/991/2016/>
- Chwala, C., Polz, J., Graf, M., Sereb, D., Blettner, N., Keis, F., & Boose, Y. (2021). *pycomlink/pycomlink: v0.3.2*. Zenodo. <https://doi.org/10.5281/zenodo.4810169>
- D'Amico, M., Manzoni, A., & Solazzi, G. L. (2016). Use of operational microwave link measurements for the tomographic reconstruction of 2-D maps of accumulated rainfall. *IEEE Geoscience and Remote Sensing Letters*, 13(12), 1827–1831. <http://ieeexplore.ieee.org/document/7592404/>
- de Vos, L. W., Overeem, A., Leijnse, H., & Uijlenhoet, R. (2019). Rainfall estimation accuracy of a nationwide instantaneously sampling commercial microwave link network: Error dependency on known characteristics. *Journal of Atmospheric and Oceanic Technology*, 36(7), 1267–1283. <https://journals.ametsoc.org/view/journals/atot/36/7/jtech-d-18-0197.1.xml>
- Goldshtein, O., Messer, H., & Zinevich, A. (2009). Rain rate estimation using measurements from commercial telecommunications links. *IEEE Transactions on Signal Processing*, 57(4), 1616–1625. <http://ieeexplore.ieee.org/document/4749357/>
- Graf, M., Chwala, C., Polz, J., & Kunstmann, H. (2020). Rainfall estimation from a German-wide commercial microwave link network: Optimized processing and validation for 1 year of data. *Hydrology and Earth System Sciences*, 24(6), 2931–2950. <https://hess.copernicus.org/articles/24/2931/2020/>
- Graf, M., El Hachem, A., Eisele, M., Seidel, J., Chwala, C., Kunstmann, H., & Bárdossy, A. (2021). Rainfall estimates from opportunistic sensors in Germany across spatio-temporal scales. *Journal of Hydrology: Regional Studies*, 37, 100883. <https://doi.org/10.1016/j.ejrh.2021.100883>
- Haese, B., Hörning, S., Chwala, C., Bárdossy, A., Schalge, B., & Kunstmann, H. (2017). Stochastic reconstruction and interpolation of precipitation fields using combined information of commercial microwave links and rain gauges. *Water Resources Research*, 53(12), 10740–10756. <https://doi.org/10.1002/2017WR021015>
- Heistermann, M., Jacobi, S., & Pfaff, T. (2013). Technical Note: An open source library for processing weather radar data (*wradlib*). *Hydrology and Earth System Sciences*, 17(2), 863–871. <https://hess.copernicus.org/articles/17/863/2013/>
- Hörning, S. (2022). *Sebastianhoerning/RMWSPy: RMWSPy v1.2*. Zenodo. <https://doi.org/10.5281/zenodo.7048941>
- Hörning, S., & Blettner, N. (2022). *nblettner/RMWSPy: v1.1.1*. Zenodo. <https://doi.org/10.5281/zenodo.7049826>
- Hörning, S., & Haese, B. (2021). RMWSPy (v 1.1): A Python code for spatial simulation and inversion for environmental applications. *Environmental Modelling & Software*, 138, 104970. <https://linkinghub.elsevier.com/retrieve/pii/S136481522100013X>
- Hörning, S., Sreekanth, J., & Bárdossy, A. (2019). Computational efficient inverse groundwater modeling using Random Mixing and Whittaker–Shannon interpolation. *Advances in Water Resources*, 123, 109–119. <https://doi.org/10.1016/j.advwatres.2018.11.012>
- Leijnse, H., Uijlenhoet, R., & Stricker, J. N. M. (2007). Rainfall measurement using radio links from cellular communication networks. *Water Resources Research*, 43(3), W03201. <https://doi.org/10.1029/2006WR005631>
- Messer, H. (2006). Environmental monitoring by wireless communication networks. *Science*, 312(5774), 713. <https://www.sciencemag.org/lookup/doi/10.1126/science.1120034>
- Murphy, B., Müller, S., & Yurchak, R. (2021). *Geostat-framework/PyKrig: v1.6.1*. Zenodo. <https://doi.org/10.5281/zenodo.5380342>
- Overeem, A., Leijnse, H., & Uijlenhoet, R. (2013). Country-wide rainfall maps from cellular communication networks. *Proceedings of the National Academy of Sciences*, 110(8), 2741–2745. <http://www.pnas.org/cgi/doi/10.1073/pnas.1217961110>
- Overeem, A., Leijnse, H., & Uijlenhoet, R. (2016). Retrieval algorithm for rainfall mapping from microwave links in a cellular communication network. *Atmospheric Measurement Techniques*, 9(5), 2425–2444. <https://doi.org/10.5194/amt-9-2425-2016>
- Pollock, M. D., O'Donnell, G., Quinn, P., Dutton, M., Black, A., Wilkinson, M. E., et al. (2018). Quantifying and mitigating wind-induced undercatch in rainfall measurements. *Water Resources Research*, 54(6), 3863–3875. <https://doi.org/10.1029/2017WR022421>
- Polz, J., Chwala, C., Graf, M., & Kunstmann, H. (2020). Rain event detection in commercial microwave link attenuation data using convolutional neural networks. *Atmospheric Measurement Techniques*, 13(7), 3835–3853. <https://amt.copernicus.org/articles/13/3835/2020/>
- Radanovics, S., Vidal, J.-P., & Sauquet, E. (2018). Spatial verification of ensemble precipitation: An ensemble version of SAL. *Weather and Forecasting*, 33(4), 1001–1020. <https://journals.ametsoc.org/doi/10.1175/WAF-D-17-0162.1>
- Roversi, G., Alberoni, P. P., Fornasiero, A., & Porcù, F. (2020). Commercial microwave links as a tool for operational rainfall monitoring in Northern Italy. *Atmospheric Measurement Techniques*, 13(11), 5779–5797. <https://amt.copernicus.org/articles/13/5779/2020/>
- Werner, P. C., & Gerstengarbe, F.-W. (2010). *Katalog der großwetterlagen europas (1881-2009)*. Friedrich-Wilhelm Gerstengarbe.
- Wernli, H., Paulat, M., Hagen, M., & Frei, C. (2008). SAL—A novel quality measure for the verification of quantitative precipitation forecasts. *Monthly Weather Review*, 136(11), 4470–4487. <http://journals.ametsoc.org/doi/10.1175/2008MWR2415.1>
- Zinevich, A., Alpert, P., & Messer, H. (2008). Estimation of rainfall fields using commercial microwave communication networks of variable density. *Advances in Water Resources*, 31(11), 1470–1480. <https://linkinghub.elsevier.com/retrieve/pii/S030917080800050X>